

Effects of Enzyme–Ligand Interactions on the Photoisomerization of a Light-Regulated Chemotherapeutic Drug

Ruibin Liang* and Amirhossein Bakhtiari



Cite This: <https://doi.org/10.1021/acs.jpcb.1c10819>



Read Online

ACCESS |



Metrics & More

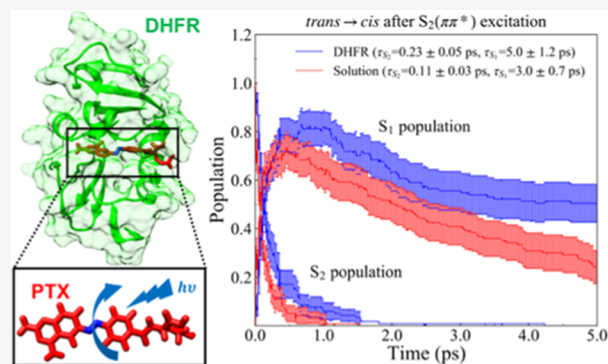


Article Recommendations



Supporting Information

ABSTRACT: Molecular photoswitches permit using light to control protein activity with high spatiotemporal resolutions, thereby alleviating the side effects of conventional chemotherapy. However, due to the challenges in probing ultrafast photoisomerization reactions in biological environments, it remains elusive how the protein influences the photochemistry of the photoswitches, which hampers the rational design of light-regulated therapeutics. To overcome this challenge, we employed first-principles nonadiabatic dynamics simulations to characterize the photodynamics of the phototretate (PTX), a recently developed photoswitchable anticancer chemotherapeutic that reversibly inhibits its target enzyme dihydrofolate reductase (DHFR). Our simulations show that the protein environment impedes the *trans* to *cis* photoisomerization of the PTX. The confinement in the ligand-binding cavity slows down the isomerization kinetics and quantum yield of the photoswitch by reshaping its conical intersection, increasing its excited-state free-energy barrier and quenching its local density fluctuations. Also, the protein environment results in a suboptimal binding mode of the photoproduct that needs to undergo large structural rearrangement to effectively inhibit the enzyme. Therefore, we predict that the PTX's *trans* → *cis* photoisomerization in solution precedes its binding with the protein, despite the favorable binding energy of the *trans* isomer. Our findings highlight the importance of the protein environment on the photochemical reactions of the molecular photoswitches. As such, our work represents an important step toward the rational design of light-regulated drugs in photopharmacology.



INTRODUCTION

Reversible, spatial, and temporal control over protein's structure and function through non-native small molecules have significant implications in minimizing the side effects of chemotherapy.^{1–4} Compared to traditional chemical tools, molecular photoswitches are unsurpassed in their ability to achieve this goal via light-controlled isomerization reactions (Figure 1A), making them promising light-regulated drugs.^{3,5–12} As such, the design and synthesis of novel molecular photoswitches have led to the rapid expansion of the field of photopharmacology.^{3,5–12} For example, dihydrofolate reductase (DHFR) has been an essential drug target to treat cancer because its inhibition interrupts the folate metabolism and leads to the death of cancer cells.¹³ Methotrexate (MTX) is an effective inhibitor of DHFR and thus a widely prescribed chemotherapeutic drug to treat cancer. However, the ubiquity of DHFR in healthy cells often leads to severe side effects of MTX such as nausea, joint pain, vomiting, and diarrhea. Therefore, to alleviate the side effect of chemotherapy, there is an urgent need to design new DHFR inhibitors with minimal side effects. The molecular photoswitch phototretate (PTX) was recently designed as a photochromic analog of the MTX.¹² The *trans* isomer of the PTX has a lower binding affinity with DHFR than its *cis*

isomer, and therefore the *trans* → *cis* photoisomerization promotes the binding of the ligand with the protein. Thus, the PTX can reversibly inhibit the DHFR enzyme with high spatial-temporal precision under the control of light (Figure 1A),¹² which can mitigate its side effect compared to the MTX.

Despite the molecular photoswitches' successful applications in photopharmacology, their design often involves expensive trial-and-error experiments.¹² Therefore, the rational design of more effective photoswitchable drugs is necessary. However, several fundamental questions remain unanswered regarding the interactions among the protein, the photoswitchable ligand, and the light. For example, it was reported that the *trans* PTX's binding affinity with DHFR is only slightly less favorable than the *cis* PTX (−9.3 vs −10.8 kcal/mol).¹² The non-negligible binding affinity of the *trans* PTX raises a critical question: does the *trans* isomer first bind with the protein and

Received: December 23, 2021

Revised: March 4, 2022

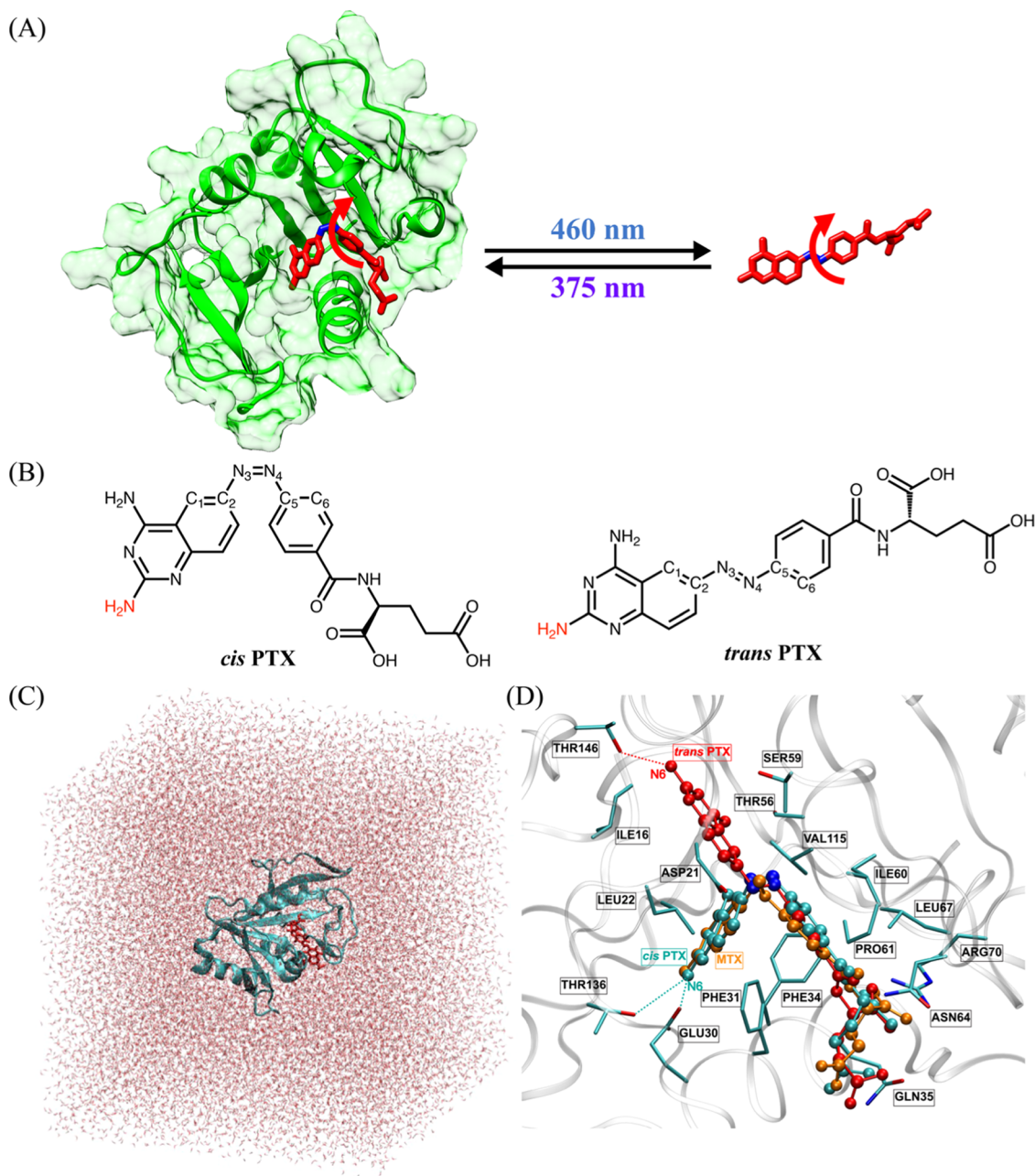


Figure 1. (A) Photoisomerization between the *cis* and *trans* PTX enables reversible inhibition of DHFR under different wavelengths of light. (B) Key atoms that define the essential torsional modes in the photoisomerization are labeled in the chemical structures of the *cis* and *trans* PTX. (C) Simulation setup for the *trans* PTX (red licorice) bound to DHFR (green ribbons) solvated in water (red dots). (D) The active site of the DHFR enzyme. The MTX in the crystal structure is shown as orange stick and balls. The *cis* and *trans* PTX obtained by docking simulation are shown in cyan and red stick and balls, respectively. The N=N double bonds in the two isomers are colored in blue. The *cis* PTX overlaps well with the MTX. There is good structural overlap between the *cis* and *trans* PTX on the benzamido moiety side of the N=N bond, but these two structures differ significantly on the other side of the double bond: the N6 atom in the *cis* PTX (red atom in panel B) is hydrogen bonded to the Glu30 and Thr136 (cyan dashed lines), whereas the same atom in the *trans* isomer is hydrogen bonded to the Thr146 (red dashed line).

then undergo the *trans* → *cis* photoisomerization, or is the reverse sequence of events more probable? Additionally, it remains unclear how the protein environment affects the photoisomerization kinetics and quantum yield (QY) of the photoswitches. Answering these questions at molecular-level detail is crucial to the successful design of next-generation light-regulated drugs for cancer treatment.

Molecular simulation is indispensable to achieving this goal because it can reveal the energetics and kinetics of biochemical reactions at atomic-level detail, which is often beyond the limit

of current experimental techniques. However, it is challenging to use computational methods to study photochemical reactions in proteins. First, traditional classical dynamics cannot describe the nonadiabaticity of photodynamics involving population transfer among different electronic states. Hence, accurate nonadiabatic dynamics methods are necessary to propagate the coupled nuclear and electronic degrees of freedom according to the time-dependent Schrödinger's equation. However, such simulations often demand expensive computational costs. Second, the accuracy of nonadiabatic

dynamics simulations also depends on the calculations of the potential energy surfaces (PES) and nonadiabatic couplings (NAC) of the electronic states, and it is essential to employ first-principles electronic structure methods that include both static and dynamic correlations.^{14,15} However, most first-principles electronic structure methods fulfilling these requirements are usually too expensive to afford “on-the-fly” nonadiabatic dynamics simulations. These computational challenges result in a general lack of understanding of how the confinement imposed by the biomolecules impacts the photodynamics of molecular photoswitches.

As a first step to overcome these challenges, in this work, we employed first-principles nonadiabatic dynamics simulations to probe the effects of protein–ligand interactions on the *trans* → *cis* photoisomerization of the PTX. The nonadiabatic molecular dynamics simulations were performed using the *ab initio* multiple spawning (AIMS)^{16–18} algorithm coupled with “on-the-fly” first-principles electronic structure calculations using the hole–hole Tamm–Dancoff-approximated density functional theory (hh-TDA–DFT).¹⁴ The hh-TDA–DFT method incorporates both the static and dynamic electron correlations that are essential for the accurate description of the PES and NACs.^{14,15,19} The accuracy of the hh-TDA–DFT method has been systematically benchmarked against high-level *ab initio* calculations and experiments.^{14,19–21} The AIMS algorithm is a computationally efficient and accurate nonadiabatic dynamics method for evolving the nuclear wave packets on coupled electronic states according to time-dependent Schrödinger’s equation.^{16–18} It uses trajectory basis functions (TBF) to represent the evolution of nuclear wave functions, which significantly boosts its computational efficiency.^{16–18} Although a few simulation studies have investigated the photodynamics of azobenzene in biological systems,^{22–24} they employed more approximate simulation methods than the current study. Specifically, the electronic structure was treated with either semiempirical methods^{22,23} or *ab initio* methods that lack dynamic electron correlation.²⁴ In addition, the nonadiabatic dynamics was simulated by the surface-hopping method,²⁵ which suffers from the overcoherence issue²⁶ that has not been fully resolved by the decoherence corrections without introducing new problems.^{27,28} By comparison, the combination of the hh-TDA–DFT and AIMS methods in the current study offers a more accurate description of the photodynamics of the azobenzene derivatives. These state-of-the-art computational approaches enable us to gain deep insights into the effects of the protein environment on the photochemical reactions of the molecular photoswitches, which will be discussed in detail below.

METHOD

This section details the procedures for (1) system setup and molecular docking simulation, (2) classical molecular dynamics (MD) simulation, (3) ground-state quantum mechanics/molecular mechanics (QM/MM) MD simulation, (4) absorption spectra calculation, (5) AIMS simulation, (6) characterization of minimum energy conical intersections, and (7) excited-state umbrella sampling simulations.

System Setup and Molecular Docking Simulations. Starting from the crystal structure of DHFR (PDB code: 1U72),²⁹ the cocrystallized ligands, ions, and water molecules were first removed. The removed crystal water molecules were all on the surface of the protein and were accessible from bulk solution. They were readily regained during the subsequent

MD equilibration (see below). Thus, the removal of the crystal water molecules was not expected to largely perturb the ligand binding. The protein contained 186 amino acid residues. The missing protein hydrogen atoms were added, and the partial charges of all protein atoms were assigned based on the Amber ff14SB force field.^{30,31} All titratable residues assumed their standard protonation states (GLU, ASP: deprotonated; LYS, ARG, TYR, CYS, THR, SER: protonated; HIS: singly protonated on Ne atom). To prepare the coordinates and partial charges of the ligand PTX, the *trans* isomer was first optimized on the ground state in the vacuum using the density functional theory (DFT) with the B3LYP functional³² and 6-31G* basis set. At this B3LYP optimized geometry, the Hartree–Fock/6-31G* energy calculation was performed, and the wave function was fitted to obtain the partial charges of the PTX using the restrained electrostatic potential (RESP)³³ approach. Then, AutoDock Vina software³⁴ was used to identify the binding poses of the *trans* PTX in DHFR. The structure with the best score in a cluster of top-score structures was selected (Figure 1D). For comparison, the *cis* PTX was also docked into the protein following a similar procedure (Figure 1D). The selected *trans* PTX structure partially overlaps with the methotrexate in the crystal structure²⁹ and the docked *cis* PTX on the benzamido moiety side of the N=N bond (Figure 1D). The docked structures and the predicted binding energies (−10.4 and −9.1 kcal/mol for *cis* and *trans* isomers, respectively) agreed well with the ones in ref 12. Then, the protein–ligand complex was solvated in a box of water molecules with a periodic boundary condition of $\sim 85 \times 91 \times 96 \text{ \AA}^3$ (Figure 1C). The force field parameters of the PTX were generated using the general Amber force field (GAFF) procedure.^{35,36} The water and protein were modeled using the SPFF/Fw³⁷ and Amber ff14SB force fields,^{30,31} respectively.

To probe the effects of the protein on the photodynamics of PTX, an aqueous solution simulation system was also constructed by solvating the *trans* PTX in a box of water molecules, resulting in a periodic condition of $\sim 51 \times 53 \times 59 \text{ \AA}^3$.

Classical MD Equilibration. The coordinates of the system were first optimized while restraining the heavy atoms of the protein and ligand using harmonic potential with $100 \text{ kcal/mol/\AA}^2$ force constant. Next, the system was equilibrated for 10 ps in the constant NVT ensemble at a temperature of 300 K, followed by 5 ns equilibration in the NPT ensemble at the same temperature and 1 atm pressure, where the force constants of the restraints were gradually reduced to zero. Then, 50 ns simulation was performed in the constant NPT ensemble without any restraints. The first 10 ns of the trajectory was discarded as equilibration, and the last 40 ns of the trajectory was treated as a production run. A Langevin thermostat with a friction coefficient of 1 ps^{-1} and a Monte Carlo barostat with an attempt frequency of 100 steps was used to maintain the temperature and pressure, respectively. A time step of 1 fs was used to propagate the dynamics. A 12 \AA cutoff was used for nonbonded interactions, and electrostatic interactions were calculated using the particle mesh Ewald (PME) method. The PTX remained in the enzyme cavity during the 40 ns simulation. The classical MD simulations of the *trans* PTX in the aqueous solution followed the same procedures as the protein–ligand systems, except that no restraint on the protein was involved. All of the classical MD simulations were performed with the OPENMM software package.³⁸

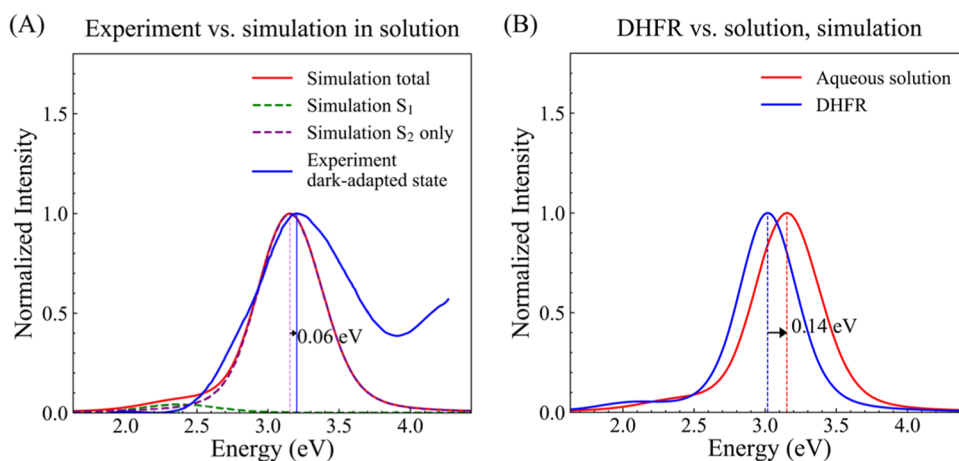


Figure 2. (A) Calculated absorption spectrum (solid red line) of the *trans* PTX in the aqueous solution agrees well with the experiment (solid blue line). The contributions from the $S_0 \rightarrow S_1$ and $S_0 \rightarrow S_2$ excitations to the calculated spectrum are in green and purple dashed lines, respectively. The peaks of the experimental and calculated spectra are labeled by the vertical lines. The experimental and calculated wavelengths of maximum absorption for the $S_0 \rightarrow S_2$ excitation are 386.7 nm (3.21 eV) and 393.6 nm (3.15 eV), respectively. (B) Protein environment in DHFR slightly blue-shifts the absorption maximum of *trans* PTX by 0.14 eV compared to the aqueous solution. However, the absorption spectra in the solution and DHFR still have significant overlap, justifying the comparison of the PTX's photodynamics following the S_2 excitation in these two distinct environments under the same wavelength of excitation (375 nm).

Ground-State QM/MM Dynamics. To prepare for the AIMS simulation and absorption spectra calculations, we need to sample the system's conformations in the Franck–Condon (FC) region. Because both types of calculations employ the hh-TDA–DFT method to describe the PTX's PES (see below), it is essential to sample the FC structures with a consistent Hamiltonian. Although the GAFF description of the PTX ligand enabled efficient MD equilibration, it was less accurate than the *ab initio* method for sampling the geometry of the nonstandard ligand. For example, during the MD equilibration, the two torsions nearby the central N=N bond ($C_1 = C_2 - N_3 = N_4$ and $N_3 = N_4 - C_5 = C_6$, abbreviated as θ_{CCNN} and θ_{NNCC} below) sometimes deviated from 180° by up to 60° . This distorted the central planar structure of the *trans* PTX, and was an artifact arising from the inaccuracy of the force field. Because the hh-TDA–DFT is in good agreement with standard restricted DFT near the FC region,¹⁴ we employed ground-state QM/MM MD simulations with DFT as the QM method to adjust the geometries of the PTX sampled from the classical force-field-based MD simulation. From the classical MD trajectory, 40 snapshots were extracted evenly with 1 ns time interval. For each snapshot, a subsystem with an open boundary condition was created and used as one of the starting structures for the QM/MM simulations. This is due to the current limitation of the TeraChem software package^{39–42} in treating the PBC in the QM/MM simulations. The subsystem includes the protein, ligand, and every water molecule that has at least one atom within 10 Å of any atom in the protein–ligand complex. Then, for each subsystem, a QM/MM MD trajectory was initiated and propagated on the ground state in the constant NVT ensemble at 300 K temperature using a Langevin thermostat. Each QM/MM trajectory was propagated for ~ 7 ps on the ground state with a time step of 0.5 fs. As a result, ~ 350 ps QM/MM dynamics were propagated in total, which originated from 40 ns MM conformational sampling of the ligand–protein complex. In all of the QM/MM equilibrated structures, the θ_{CCNN} and θ_{NNCC} of the *trans* PTX deviated less than 40° from 180° , which indicates that the ground-state QM/MM dynamics partially

restored the central planarity of the ligand. As mentioned above, such geometric adjustment is necessary for correctly launching the subsequent AIMS dynamics and absorption spectra calculations.

In the ground-state QM/MM MD simulations, the QM region included only the PTX, while the MM region included the rest of the system. The QM and MM regions were coupled by the electrostatic embedding scheme, where the electronic density of the QM atoms interacts with the fixed point charges on the MM atoms. We chose such a QM region to balance the accuracy and efficiency. The PTX is not covalently bonded to any protein atoms. It is hydrogen bonded with only 1–2 neighboring residues (Figure 1D), and its van der Waals interactions with the protein can be treated reliably by MM force field. Furthermore, it is well known that the photoexcitation of *trans* azobenzene to the lowest excited states (S_1 and S_2) is localized near the central azo moiety.^{19,43} Thus, the inclusion of only the PTX in the QM region is justifiable, which has been done in a number of nonadiabatic dynamics simulation studies of photoactive proteins as reviewed in ref 44. The QM region was treated with B3LYP/6-31G*, and the MM region was treated with the same force fields as described in the previous sections. The QM/MM simulations for the *trans* PTX in the aqueous solution were also performed following the same procedures. The TeraChem^{39–42} interfaced with the OPENMM packages³⁸ was used to perform the ground-state QM/MM simulations.

Absorption Spectra Calculation. From each of the 40 QM/MM trajectories, snapshots were extracted from the last 5 ps with a time interval of 10 fs, resulting in 20,000 snapshots in total. For each snapshot, excitation energies and oscillator strengths for $S_0 \rightarrow S_1$ ($n\pi^*$) and $S_0 \rightarrow S_2$ ($\pi\pi^*$) transitions were calculated using the QM/MM approach with the same partitioning scheme as the MD simulation. The QM region was treated with the hh-TDA–DFT method with B3LYP functional and 6-31G* basis set (hh-TDA–B3LYP/6-31G*) and the MM region with the same force fields as mentioned above. The absorption spectra were then calculated following ref 45, and Lorentzian functions were used to convolve the

cross section in energy with a full width at half-maximum (FWHM) of 0.15 eV.

AIMS Simulation. The PTX's *trans* \rightarrow *cis* isomerization was induced by illumination at 375 nm in the experiment.¹² This wavelength corresponds to the $S_0 \rightarrow S_2$ ($\pi\pi^*$) initial excitation (Results and Discussion). The AIMS simulations were prepared accordingly. In particular, 40 initial conditions (ICs, i.e., the initial coordinates and momenta of the TBFs' centroids) were taken from the last snapshots of the 40 ground-state QM/MM trajectories. According to our calculated absorption spectra (Figure 2A,B), the TBFs were initially placed on the S_2 state. The TBFs were then propagated and spawned according to the full multiple spawning (FMS) algorithm.^{16–18} The quantities required for the FMS simulation, such as energies, gradients, and nonadiabatic couplings of S_0 , S_1 , and S_2 states, were calculated on the fly using the hh-TDA–B3LYP/6-31G* method. The stochastic-selection AIMS (SS-AIMS) method⁴⁶ was employed to speed up the simulation while maintaining accuracy.²⁷ The TBF overlap threshold to trigger stochastic selection was set to $\sim 10^{-3}$.²⁰ In the SS-AIMS simulations, three reruns with different random seeds were performed for each IC. For each IC, the simulation was terminated after more than 95% of the TBFs' population had decayed to the ground state or when the simulation time had reached 5 ps. The S_1 and S_2 states' relaxation time constants (τ_{S_1}) and (τ_{S_2}) were fitted using the following first-order kinetics model

$$P_{S_2}(t) = \exp\left(-\frac{t}{\tau_{S_2}}\right) \quad (1)$$

$$P_{S_1}(t) = \frac{\tau_{S_1}}{\tau_{S_1} - \tau_{S_2}} \left[\exp\left(-\frac{t}{\tau_{S_1}}\right) - \exp\left(-\frac{t}{\tau_{S_2}}\right) \right] \quad (2)$$

The error bars in the relaxation time constants were obtained by bootstrapping over 1000 random samples with replacement for the 40 ICs.

The photoisomerization QY was calculated based on the centroid geometries and populations of the ground-state TBFs that have been successfully spawned during the AIMS simulation within 5 ps. In particular, each ground-state TBFs was propagated for ~ 100 fs after it was decoupled from the S_1 state. The decoupling was defined as when the dot product of the centroid's velocity with the S_1/S_0 derivative coupling vector decreased below 0.01 a.u. Then, the centroids of the TBFs were minimized on the ground state. If the absolute value of the final C2–N3 = N4–C5 torsion angle (Figure 1B) was below 40° , the population of this TBF was assigned to *cis* isomer. If the torsion angle is between 140 and 220° , the population was assigned to *trans* isomer. The choices of the cutoff values are justified by the distributions of the final torsion angles for both *cis* and *trans* isomers, which are indicated in Figure S1. All final torsion angles fell within the chosen cutoff. The QY for the *trans* \rightarrow *cis* isomerization was defined as the ratio of the total population of the *cis* isomer to the total population of all ground-state TBFs. For the SS-AIMS simulations, the QYs were averaged over three reruns. The error bars in the QYs were obtained by bootstrapping over 1000 random samples with replacement.

The AIMS simulations were performed using the FMS90 code interfaced with the TERAChem/OPENMM software packages.^{38–42}

Characterization of the Minimum Energy Conical Intersections (CI). In the AIMS simulations of DHFR and aqueous solution systems, for each ground-state TBF successfully spawned through a reactive S_0/S_1 CI (see "Results and Discussion" for definition), the *minimum energy conical intersections* (MECI) were searched starting from the spawning geometry. During the CI optimization, the atoms that were more than 4 \AA away from the PTX were kept frozen. Then, the following quantities of the MECI were calculated following the definition introduced by Yarkony⁴⁷

$$\mathbf{g} = \frac{1}{2} \left(\frac{\partial E_1}{\partial \mathbf{R}} - \frac{\partial E_0}{\partial \mathbf{R}} \right) \quad (3)$$

$$\mathbf{h} = \left\langle \phi_1 \left| \frac{\partial H}{\partial \mathbf{R}} \right| \phi_0 \right\rangle \quad (4)$$

$$\mathbf{s} = \frac{1}{2} \left(\frac{\partial E_1}{\partial \mathbf{R}} + \frac{\partial E_0}{\partial \mathbf{R}} \right) \quad (5)$$

$$s^x = \frac{\mathbf{s} \cdot \mathbf{g}}{g^2} \quad (6)$$

$$s^y = \frac{\mathbf{s} \cdot \mathbf{h}}{h^2} \quad (7)$$

E_1 and E_0 are the potential energies of S_1 and S_0 states, respectively. \mathbf{g} is the difference of the gradient vectors of the two states. \mathbf{h} is the nonadiabatic coupling vector between the two states, and because the mixing of the two electronic wave functions (ϕ_1 and ϕ_0) is arbitrary at the CI, \mathbf{g} and \mathbf{h} can be constructed as orthogonal vectors, with g and h denoting their lengths. These two vectors span the branching plane of the MECI, meaning that displacements from the MECI along these two vectors lift the energy degeneracy of the two states (Figure 5A,B). \mathbf{s} is the seam vector describing the topography, and s^x and s^y are the scaled tilt parameters quantifying the sloped/peaked character along each of the two branching plane vectors. s^x and s^y are zero for perfectly peaked (hourglass-shaped) CI and are larger for more sloped CI along the corresponding branching plane vectors.

Excited-State Umbrella Sampling Simulations. Umbrella sampling simulations were performed on the S_1 state to calculate the free-energy surfaces (FES) of the PTX in DHFR and solution, resulting in two one-dimensional potentials of mean forces (PMFs). The reaction coordinate of the PMF was the central C2–N3 = N4–C5 dihedral angle (θ_{C2N3N4C5}). For each PMF, 10 umbrella windows were placed along the reaction path, with window centers ranging from 180 to 90° with a 10° interval, and a harmonic potential with $100 \text{ kcal/mol/radian}^2$ force constant was imposed on the reaction coordinate for each window. The first umbrella window started from the last snapshot of a ground-state QM/MM MD trajectory. The initial structure of each window was obtained from the structure of its adjacent window after equilibration for ~ 1 ps. The hh-TDA–B3LYP/Amber method was used to calculate the S_1 state forces on the atoms on the fly during the umbrella sampling simulations. For each umbrella window, the sampling was performed for at least 6 ps. The first 1 ps trajectory was discarded as equilibration, and the remaining 5 ps trajectory was treated as the production run. The total excited-state QM/MM umbrella sampling time was thus 100 ps. The PMFs were calculated by unbiasing the distributions of the reaction

coordinates using the WHAM algorithm.^{48,49} The umbrella sampling simulations were performed using the TERA-CHEM^{39–42} interfaced with the OPENMM packages.³⁸

RESULTS AND DISCUSSION

Excited-State Population Decay and Quantum Yield.

In the experiment,¹² the *trans* → *cis* photoisomerization was induced by 375 nm light. Our calculated absorption spectrum in the aqueous solution (Figure 2A) quantitatively agreed with the experiment for the wavelength of maximum absorbance, with a deviation of only 0.06 eV (Figure 2A). The absorption spectrum is dominated by the $S_0 \rightarrow S_2$ excitation induced by the $\pi \rightarrow \pi^*$ transition, which has a much larger oscillator strength than the $S_0 \rightarrow S_1$ excitation induced by the $n \rightarrow \pi^*$ transition. The $S_0 \rightarrow S_2$ excitation is slightly blue-shifted by 0.14 eV in DHFR, but the absorption spectrum in DHFR still significantly overlaps with the one in the aqueous solution (Figure 2B). Therefore, we expect that the $S_0 \rightarrow S_2$ excitation will be dominant under the illumination of 375 nm in both the aqueous solution and DHFR. Based on this, we chose the S_2 state as the initial electronic state in the AIMS simulation for both environments. The time evolutions of the excited states' populations and the relaxation time constants are illustrated in Figure 3 and Table 1. The QYs for the photoisomerization in

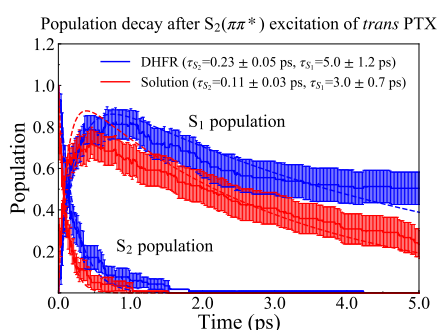


Figure 3. Excited-state population decay as a function of time for the *trans* → *cis* isomerization of the PTX following the S_2 ($\pi\pi^*$) excitation. The blue and red curves indicate the results for the PTX in DHFR and aqueous solution, respectively. The relaxation time constants of the excited states (τ_{S_1} and τ_{S_2}) are labeled in the parentheses. The protein environment has a pronounced effect in slowing down the kinetics of the *trans* → *cis* isomerization. The fits to the population decay using eqs 1 and 2 are indicated by the dashed lines.

DHFR and the aqueous solution are compared in Table 1. It is evident that the *trans* → *cis* QY is reduced from 0.31 ± 0.05 in solution to 0.15 ± 0.05 in DHFR. The PTX's isomerization QY in aqueous solution is slightly higher than that of the *trans* azobenzene induced by $S_0 \rightarrow S_2$ excitation, which was measured to be ~ 0.11 to 0.15 in solution.^{50–53} The difference in the QYs of the PTX and the azobenzene could arise from the fact that the central azo moiety (i.e., the N=N bond) is covalently linked to different functional groups, the electronic properties of which are well known to affect the isomerization QYs of the azobenzene derivatives.⁵⁴ Moreover, the S_1 and S_2 excited states have longer lifetimes in DHFR than the aqueous solutions (Figure 3 and Table 1). Although the fits to the population decay are not particularly satisfactory in certain regions (Figure 3), the difference in the excited-state lifetimes of the PTX in the two environments are beyond the error bars

Table 1. Isomerization QY, the Excited-State Lifetimes, the Average, and Variance of the PTX's Contact Number (eq 8) for the *trans* → *cis* Photoisomerization after the S_2 Excitation in DHFR and the Aqueous Solution^a

quantities	solution	DHFR
QY	0.31 ± 0.05	0.15 ± 0.05
τ_{S_1}	3.0 ± 0.7 ps	5.0 ± 1.2 ps
τ_{S_2}	0.11 ± 0.03 ps	0.23 ± 0.05 ps
\bar{N}	148 ± 1	134 ± 1
$\overline{\sigma_N^2}$	119 ± 5	73 ± 5

^aIn each system, the QYs are averaged over the ICs that have successfully spawned S_0 TBFs within 5 ps. The lifetimes τ_{S_1} and τ_{S_2} are fitted to the time evolution of excited-state populations averaged over all 40 ICs. The average and variance of the contact number (\bar{N} and $\overline{\sigma_N^2}$) are averaged over all S_1 TBFs that decay through the reactive S_0/S_1 CI. The error bar for each quantity was estimated by bootstrapping over 1000 random samples of the original data set (e.g., ICs or TBFs) with replacement.

(Table 1). Overall, the above analysis indicates that the protein environment impedes the *trans* → *cis* photoisomerization of the PTX in terms of both QY and reaction kinetics.

Origin of the Reduced Isomerization Quantum Yield in DHFR. To understand the origin of the lowered QY in DHFR, we categorized the $S_1 \rightarrow S_0$ nonradiative decay by the type of the S_0/S_1 conical intersection (CI) through which the population transfer occurs (Figure 4A,B). Similar to the azobenzene's photodynamics,^{14,19,20} the PTX's S_1 state population can decay to the S_0 state through either the unreactive or reactive S_0/S_1 CIs (Figure 4C,D), which belong to the same crossing seam.^{55–57} The unreactive CI features a near planar geometry with the central $C_2-N_3 = N_4-C_5$ dihedral angle (θ_{CNNC}) close to 180° and large $C_2-N_3 = N_4$ and $N_3 = N_4-C_5$ bending angles (α_{CNN} and α_{NNC}) beyond 140° (Figure 4C). The nonradiative decay through this type of CI exclusively generates the *trans* isomer because there is no rotation around the θ_{CNNC} . In contrast, the reactive CI features a near perpendicular geometry with θ_{CNNC} close to 90° (Figure 4D). The nonradiative decay through this type of CI will have some possibility to successfully generate the *cis* isomer product due to the rotation of θ_{CNNC} . The unreactive CI is energetically higher than the reactive CI by 0.78 eV in the vacuum. As a result, the former can only be accessed in the initial stage of the photodynamics when the high kinetic energy released from the $S_2 \rightarrow S_1$ relaxation has not been fully dissipated to the environment.²⁰ Thus, the $S_1 \rightarrow S_0$ decay through the reactive CI on average occurs at a longer timescale than the unreactive CI (1.9 ± 0.2 vs 0.9 ± 0.1 ps in DHFR and 2.2 ± 0.2 vs 0.4 ± 0.1 ps in solution, estimated from AIMS simulations up to 5 ps). Indeed, after 2.5 ps of photoexcitation, the $S_1 \rightarrow S_0$ decay is exclusively through the reactive CI.

Our population transfer analysis (Figure 4A,B) indicates that the molecular environment around the PTX impacts the *cis:trans* branching ratio after the system decays through the reactive S_0/S_1 CI. Specifically, in DHFR, $15\% + 49\% = 64\%$ of the total S_0 population arises from $S_1 \rightarrow S_0$ decay through the reactive CI, and 15% of the total S_0 population eventually ends up as the *cis* isomer. Out of all population decaying through the reactive CI, the probability to generate the *cis* isomer (or branching ratio) is $15\% / (15\% + 49\%) \approx 23\%$. In contrast, in the aqueous solution $31\% + 37\% = 68\%$ of the total S_0

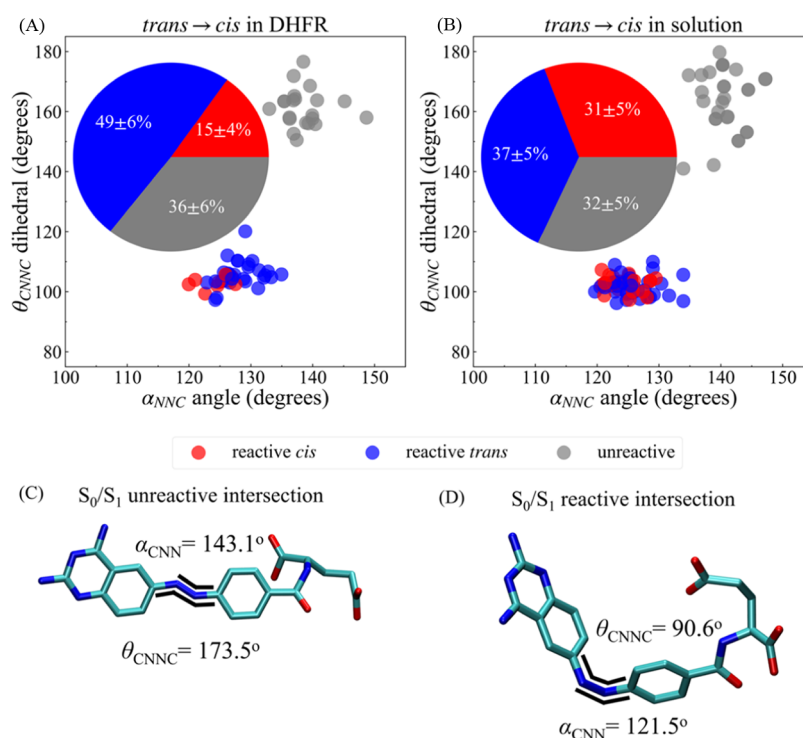


Figure 4. (A, B) Decomposition of population decay through the unreactive and reactive S_0/S_1 CIs for the PTX *trans* \rightarrow *cis* photoisomerization following the S_2 excitation in DHFR and aqueous solution, respectively. Each circle represents an S_0 state TBF, with its location determined by the TBF's centroid geometry at the spawning time, i.e., the larger one of the two C–N=N angles (α_{CNN}) and the C–N=N–C torsion (θ_{CNNC}). The circle is gray if the TBF is spawned through an S_1/S_0 unreactive CI (C) and exclusively ends up as the *trans* isomer. The circle is colored red (blue) if the S_0 TBF is spawned through a reactive S_0/S_1 CI (D) and ends up as the *cis* (*trans*) isomer. The pie charts in the insets indicate the relative populations of the S_0 TBFs in each of the three categories. The structures of the unreactive and reactive minimum energy CIs (MECI) were optimized in the gas phase and are similar to those encountered in DHFR and the aqueous solution. The uncertainties are estimated as one standard error using bootstrapping with 1000 samples.

population arises from $S_1 \rightarrow S_0$ decay through the reactive CI, and 31% of the total S_0 population ends up as the *cis* isomer. Out of all population decaying through the reactive CI, the branching ratio of the *cis* isomer is $31\% / (31\% + 37\%) \approx 46\%$. Therefore, the difference in the branching ratio through the reactive S_0/S_1 CI (23% in DHFR vs 46% in solution) contributes to the different QYs in these two systems.

Admittedly, our AIMS simulations were not propagated until full depletion of the excited-state populations due to resource limitations. After 5 ps, 50 and 76% of the excited-states' population has decayed to S_0 state in DHFR and the solution, respectively. However, the conclusion from the above analysis will not be changed much by further extending our simulations. This is because it is reasonable to assume that after 5 ps all of the remaining S_1 populations (50% for DHFR and 24% for aqueous solution) will eventually decay through the reactive S_0/S_1 CI with the same branching ratio as the first 5 ps. Based on this assumption, we estimate that the final QY in DHFR will be $15\% \times 50\% + 23\% \times 50\% = 0.19$, and the final QY in the solution will be $31\% \times 76\% + 46\% \times 24\% = 0.35$. The estimated QYs confirm our observation that a lower branching ratio of the reactive CI leads to a reduced QY in DHFR as compared to the aqueous solution.

The different branching ratios of the reactive CIs in DHFR and the solution suggest that the protein environment shapes the topography of the reactive S_0/S_1 CI to make it less productive for generating the *cis* isomer. To test this hypothesis, we further characterized the topography of the reactive S_0/S_1 MECIs in DHFR and the solution (Table 2 and

Table 2. Average Values of s^x and s^y Parameters (eqs 6 and 7) Depicting the Topography of the Reactive S_0/S_1 CI of PTX in the Aqueous Solution and DHFR

CI parameters	solution	DHFR
$\overline{s^x}$	0.33 ± 0.03	0.47 ± 0.05
$\overline{s^y}$	$(6 \pm 5) \times 10^{-5}$	$(1.1 \pm 0.2) \times 10^{-6}$

Figure 5A,B). As shown in Table 2, the MECIs in the DHFR environment have larger s^x on average (eq 6) than in the aqueous solution. The larger s^x indicates that the MECIs in DHFR are more sloped along the g vector than those in the aqueous solution. A visual inspection of the MECIs in the two environments (Figure 5A,B) confirms such observation. The g vector is approximately in line with the direction of the N=N bond rotation (Figure 5C). The more sloped MECI will generally lead to a reduced QY.⁵⁸ Therefore, the DHFR's protein environment reduces the photoisomerization QY by changing the topography of the reactive S_0/S_1 CI.

Origin of the Slowdown of Isomerization Kinetics in DHFR. To further understand the effect of the environment on the kinetics of the nonradiative decay, we performed umbrella sampling simulations with the hh-TDA–B3LYP/Amber method and calculated the S_1 state PMFs for the PTX's isomerization in both DHFR and the aqueous solution (Figure 6). The PMFs were calculated along the rotation of θ_{CNNC} , which is key to photoisomerization. In the aqueous solution, the rotation around θ_{CNNC} from the planar geometry ($\sim 180^\circ$) to the near perpendicular geometry around the CI ($\sim 90^\circ$) only

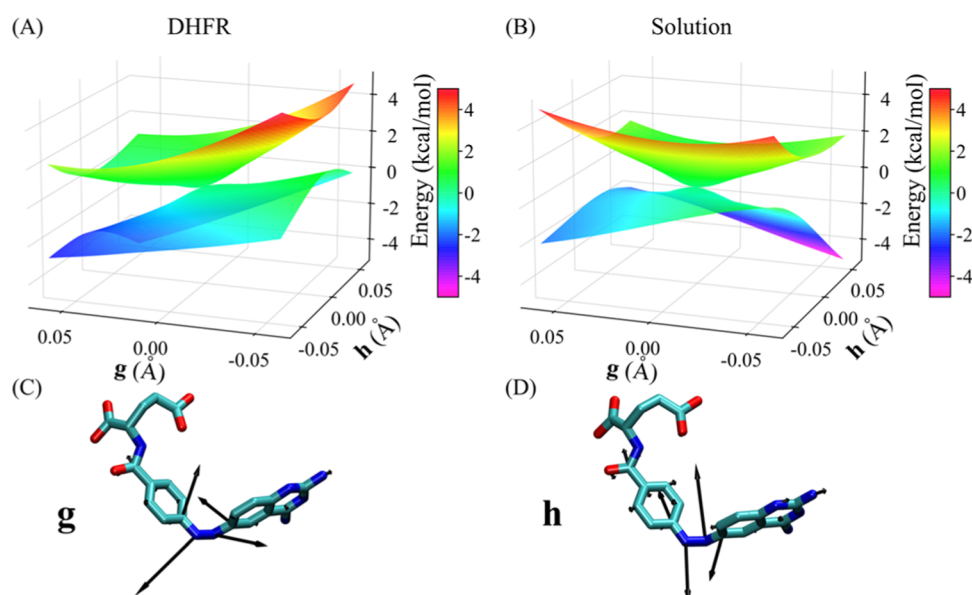


Figure 5. Topography of the reactive S_0/S_1 MECI in (A) DHFR and the (B) aqueous solution. The protein environment makes the MECI more sloped along the g vector than the aqueous solution. (C, D) g and h vectors (black arrows) spanning the CI plane for the reactive S_0/S_1 MECI. The Franck–Condon point is projected on the two-dimensional CI plane at 0.13 and 0.20 Å along the g and h vectors, respectively.

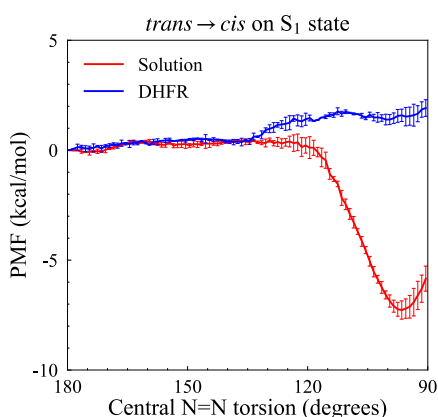


Figure 6. Potential of mean forces (PMFs) for the rotation of θ_{CNNC} on the S_1 state in the aqueous solution (red) and DHFR (blue). The protein environment increases the free-energy barrier to access the reactive S_0/S_1 CI and slows down the $trans \rightarrow cis$ photoisomerization. The error bars were estimated by block averaging analysis of the QM/MM trajectories of the umbrella windows.

needs to overcome a small free-energy barrier of ~ 0.5 kcal/mol (Figure 6), and the process is exergonic with a $\Delta G = -7.3$ kcal/mol. In contrast, in DHFR, the rotation around θ_{CNNC} needs to overcome a larger barrier of 1.7 kcal/mol, and the process is endergonic with $\Delta G = 1.7$ kcal/mol (Figure 6). As mentioned above, the reactive CI is the major channel for the $S_1 \rightarrow S_0$ decay beyond 1 ps. Although the difference in the free-energy barrier is small (1.7 vs 0.5 kcal/mol), such difference is above the errors bars of our free-energy calculations estimated by block averaging analysis. Additionally, the qualitative difference of the two PMFs (exergonic vs endergonic) is well beyond the statistical uncertainty of the PMFs. In a recent study authored by one of us,⁵⁹ similar method was used to estimate the effect of protein mutation on the excited-state free-energy surface of the retinal protonated Schiff base in channelrhodopsin 2. The magnitude of the difference in the free-energy barrier between the wild type and the E123T

mutant of that protein is on par with the current work and beyond the error bars of the calculation, and the amount of sampling is also similar to the current work (~ 100 ps).⁵⁹ Thus, the significant slowdown of the S_1 state population decay in DHFR can be mainly attributed to the increased S_1 state free-energy barrier that impedes the rotation of θ_{CNNC} .

The slowdown of the isomerization kinetics in the protein can also be understood in terms of the PTX's local density fluctuation, which is characterized by the variance of the PTX's contact number N defined as below⁶⁰

$$N = \sum_{i \in A} \sum_{j \in B} \frac{1 - [(r_{ij} - d_0)/r_0]^6}{1 - [(r_{ij} - d_0)/r_0]^{12}} \quad (8)$$

The A and B are the sets of atoms comprising the PTX molecule and the rest of the system, respectively. r_{ij} is the distance between a particular pair of atoms from the PTX and its environment. $d_0 = 2.5$ Å and $r_0 = 0.5$ Å. With these parameters, N effectively counts the number of atoms in the environment located 2–3 Å away from the PTX.⁶⁰ For each S_1 state TBF that encountered a reactive S_0/S_1 CI and successfully spawned the final S_0 state TBF (see “Method”), the average and variance of N (\bar{N} , σ_N^2) were calculated for the trajectory of this TBF's centroid. These quantities were averaged over all such TBFs and summarized in Table 1. It is noteworthy that the σ_N^2 is lower in DHFR than in water, indicating that the protein scaffold reduces the fluctuation of atom density around the PTX. In other words, the protein environment imposes more rigid confinement on the PTX than the aqueous solution. A careful inspection of the $trans$ PTX in the protein provides insights into the origin of the reduced local density fluctuation (Figures 1D and 7A). The PTX is surrounded by a number of hydrophobic residues such as VAL115, ILE60, LEU67, PRO61, PHE31, PHE34, LEU22, and ILE16. In addition, after the MD equilibration, there is a slight translation of the PTX, which results in the formation of hydrogen bonds between two nitrogen atoms in the diaminopteridine moiety and the Asp145 and Thr56 residues

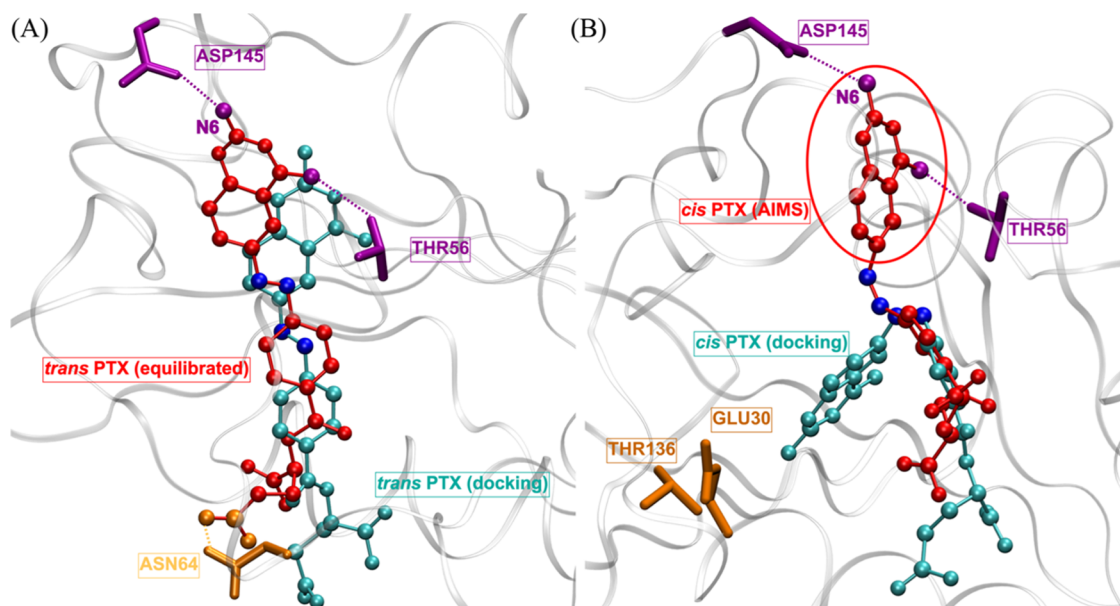


Figure 7. (A) Comparison between the *trans* PTX structure obtained by docking (cyan sticks and balls) and subsequent MD equilibration (red sticks and balls). The central N=N double bonds in the two structures are colored in blue. After MD equilibration, the *trans* PTX slightly translated in the binding cavity. The two nitrogen atoms (purple balls) in the diaminopteridine moiety of the PTX form hydrogen bonds with the ASP145 and THR56 residues (purple licorice). Also, one carboxyl group in the PTX (orange balls) flipped and formed hydrogen bonds with ASN64 residue (orange licorice). (B) Comparison between the *cis* PTX structure obtained by docking (cyan sticks and balls) and the *trans* → *cis* AIMS simulation followed by geometry optimization (red sticks and balls). The central N=N double bonds in the two structures are colored in blue. After photoisomerization from the *trans* isomer in the protein, two nitrogen atoms (purple balls) in the diaminopteridine moiety of the resulting *cis* PTX form hydrogen bonds with the ASP145 and THR56 residues (purple licorice), which is far away from the GLU30 and THR136 residues (orange licorice) that form hydrogen bonds with the *cis* PTX in the docked structure. The diaminopteridine moiety is highlighted by the red circle. In panels (A, B), protein structures after MD equilibration and AIMS simulation followed by geometry minimization are shown as gray ribbons, which are superposed on the crystal structure used for docking (omitted for clarity, protein backbone RMSD ~ 1.2–1.3 Å).

(Figure 7A). These hydrogen bonding and van der Waals interactions between the PTX and the protein residues decrease the local density fluctuation. Thus, there is a stronger caging effect in DHFR that slows down the PTX's photoisomerization kinetics, which is consistent with our free-energy calculations.

Our conclusions are consistent with the study of Mondal et al.,²² which concludes that the DNA double helix significantly slows down the *trans* → *cis* photoisomerization of the covalently incorporated azobenzene. Our conclusions are also in line with the study of Kingsland et al.,⁶⁰ which reported a positive correlation between the density fluctuation around the azobenzene and its photoisomerization QY in the DNA double helix.⁶⁰ However, the study in ref 60 was limited to the ground-state force field description of the azobenzene's dynamics. In contrast, we explicitly simulated the nonradiative decay of the excited states using first-principles nonadiabatic dynamics simulations. Hence, our data offers a more comprehensive and accurate description of the photodynamics of the azobenzene-derived photoswitches and extends the previous findings to the protein environment, which has been less studied to date. Overall, the above analysis indicates that the *trans* → *cis* photoisomerization is impeded in the protein compared to the aqueous solution. Therefore, it is more likely that the photoisomerization precedes the ligand-binding event than vice versa.

Geometry of the Cis Isomer Photoproduct in Protein.

Another noteworthy effect of the protein confinement on the photoisomerization is the binding mode of the *cis* isomer photoproduct. After *trans* → *cis* photoisomerization in the

protein, the *cis* PTX adopts a very different conformation compared to the docked *cis* isomer (Figure 7B). The *cis* PTX resulting from the photoisomerization uses its two nitrogen atoms on the diaminopteridine moiety to form hydrogen bonds with the ASP145 and THR56 residues (Figure 7B). In contrast, in the docked *cis* PTX structure, the N6 atom on diaminopteridine forms hydrogen bonds with the THR136 and GLU30 residues (Figure 1D). For the *cis* PTX resulting from the photoisomerization in DHFR, the shortest distance between the N6 atom on the diaminopteridine moiety and the two carboxyl oxygen atoms on the GLU30 is 16.2 ± 0.6 Å (averaged over all S_0 state TBFs in the *cis* isomer form). This distance is much longer than the 3.08 Å distance observed in the docked structure (Figure 1D).

The docked *cis* PTX is in the same binding mode as the MTX in the crystal structure,²⁹ which effectively inhibits the enzyme. Such a binding mode is in line with the photoswitch's design goal of mimicking the original MTX inhibitor. Therefore, the alternative binding mode of the *cis* PTX observed after the photoisomerization is likely to be suboptimal compared to the docked structure. Significant structural rearrangements need to take place to convert this suboptimal binding mode to the more favored docked structure, which may encounter large kinetic barriers given that the PTX is tightly packed in the binding site by the neighboring residues, as mentioned above. This observation further supports our conclusion that the PTX's *trans* → *cis* photoisomerization is more likely in the solution than the protein, which is followed by the ligand binding event in the *cis* isomer form.

CONCLUSIONS

In this work, we aimed to answer an essential question in photopharmacology: how do biomolecules perturb the photochemical properties of the photoswitchable drug molecules? We employed first-principles nonadiabatic dynamics simulations to understand how DHFR affects the *trans* → *cis* photoisomerization of PTX, an azobenzene-derived molecular photoswitch recently designed as an anticancer chemotherapeutic agent. We found that the *trans* → *cis* photoisomerization is impeded by the protein environment compared to the aqueous solution. The protein environment makes the reactive S_0/S_1 CI more sloped and reduces the QY. Also, it quenches local density fluctuations around the PTX and increases the excited-state free-energy barrier for the central torsion mode (θ_{CNNC}), which eventually slows down the photoisomerization kinetics. Moreover, the protein environment results in an unfavorable binding mode of the *cis* isomer photoproduct that requires large structural rearrangement to effectively inhibit DHFR. Thus, the PTX's *trans* → *cis* photoisomerization is more likely to occur in the aqueous solution before binding with DHFR, despite the *trans* isomer's non-negligible binding affinity with the enzyme.¹² Our first-principles nonadiabatic dynamics simulations thus deepen our understanding of the delicate interplay between the photoswitchable inhibitor and DHFR. Our finding has important implications for pharmacological applications: although the *trans* isomer is able to compete with the *cis* isomer for binding the protein prior to illumination, upon illumination, the *trans* isomer will not be activated to a large extent. Finally, one of the essential advantages of using photoswitches as pharmaceuticals is the reversibility of the enzyme inhibition upon illumination. Therefore, further studies of the *cis*→*trans* photoisomerization (work in progress) will still be necessary to unravel the whole picture of the photocycle underlying the interactions between DHFR, PTX, and light, which will shed light on the design principles of light-regulated therapeutics in photopharmacology.

ASSOCIATED CONTENT

Supporting Information

The Supporting Information is available free of charge at <https://pubs.acs.org/doi/10.1021/acs.jpcb.1c10819>.

Supporting Information contains Figure S1, which analyzed the distributions of the torsion around the central isomerizing N=N bond of the PTX after the AIMS simulation followed by geometry optimization (PDF)

AUTHOR INFORMATION

Corresponding Author

Ruibin Liang – Department of Chemistry and Biochemistry, Texas Tech University, Lubbock, Texas 79409, United States; orcid.org/0000-0001-8741-1520; Email: rliang@ttu.edu

Author

Amirhossein Bakhtiari – Department of Chemistry and Biochemistry, Texas Tech University, Lubbock, Texas 79409, United States

Complete contact information is available at: <https://pubs.acs.org/10.1021/acs.jpcb.1c10819>

Notes

The authors declare no competing financial interest.

ACKNOWLEDGMENTS

Ruibin Liang and Amirhossein Bakhtiari were supported by the startup funds from Texas Tech University. The authors used GPU computing facilities provided by the High-Performance Computing Center at Texas Tech University. The authors also acknowledge the helpful insights provided by Prof. Dirk Trauner in the Department of Chemistry at New York University.

REFERENCES

- (1) Fornasari, D. Pharmacotherapy for Neuropathic Pain: A Review. *Pain Ther.* **2017**, *6*, 25–33.
- (2) Kalinichenko, L. S.; Gulbins, E.; Kornhuber, J.; Müller, C. P. The role of sphingolipids in psychoactive drug use and addiction. *J. Neural Transm.* **2018**, *125*, 651–672.
- (3) Klippenstein, V.; Mony, L.; Paoletti, P. Probing Ion Channel Structure and Function Using Light-Sensitive Amino Acids. *Trends Biochem. Sci.* **2018**, *43*, 436–451.
- (4) van Beijnum, J. R.; Nowak-Sliwinska, P.; Huijbers, E. J. M.; Thijssen, V. L.; Griffioen, A. W. The Great Escape; the Hallmarks of Resistance to Antiangiogenic Therapy. *Pharmacol. Rev.* **2015**, *67*, 441.
- (5) Hüll, K.; Morstein, J.; Trauner, D. In Vivo Photopharmacology. *Chem. Rev.* **2018**, *118*, 10710.
- (6) Broichhagen, J.; Frank, J. A.; Trauner, D. A Roadmap to Success in Photopharmacology. *Acc. Chem. Res.* **2015**, *48*, 1947–1960.
- (7) Tochitsky, I.; Kienzler, M. A.; Isacoff, E.; Kramer, R. H. Restoring Vision to the Blind with Chemical Photoswitches. *Chem. Rev.* **2018**, *118*, 10748–10773.
- (8) Brechun, K. E.; Arndt, K. M.; Woolley, G. A. Strategies for the photo-control of endogenous protein activity. *Curr. Opin. Struct. Biol.* **2017**, *45*, 53–58.
- (9) Szymański, W.; Beierle, J. M.; Kistemaker, H. A. V.; Velema, W. A.; Feringa, B. L. Reversible Photocontrol of Biological Systems by the Incorporation of Molecular Photoswitches. *Chem. Rev.* **2013**, *113*, 6114–6178.
- (10) Mart, R. J.; Allemann, R. K. Azobenzene photocontrol of peptides and proteins. *Chem. Commun.* **2016**, *52*, 12262–12277.
- (11) Gautier, A.; Gauron, C.; Volovitch, M.; Bensimon, D.; Jullien, L.; Vriza, S. How to control proteins with light in living systems. *Nat. Chem. Biol.* **2014**, *10*, 533.
- (12) Matera, C.; Gomila, A. M. J.; Camarero, N.; Libergoli, M.; Soler, C.; Gorostiza, P. Photoswitchable Antimetabolite for Targeted Photoactivated Chemotherapy. *J. Am. Chem. Soc.* **2018**, *140*, 15764–15773.
- (13) Vander Heiden, M. G. Targeting cancer metabolism: a therapeutic window opens. *Nat. Rev. Drug Discovery* **2011**, *10*, 671–684.
- (14) Yu, J. K.; Bannwarth, C.; Hohenstein, E. G.; Martínez, T. J. Ab Initio Nonadiabatic Molecular Dynamics with Hole–Hole Tamm–Dancoff Approximated Density Functional Theory. *J. Chem. Theory Comput.* **2020**, *16*, 5499–5511.
- (15) Bannwarth, C.; Yu, J. K.; Hohenstein, E. G.; Martínez, T. J. Hole–hole Tamm–Dancoff-approximated density functional theory: A highly efficient electronic structure method incorporating dynamic and static correlation. *J. Chem. Phys.* **2020**, *153*, No. 024110.
- (16) Ben-Nun, M.; Quenneville, J.; Martínez, T. J. Ab Initio Multiple Spawning: Photochemistry from First Principles Quantum Molecular Dynamics. *J. Phys. Chem. A* **2000**, *104*, 5161–5175.
- (17) Curchod, B. F. E.; Martínez, T. J. Ab Initio Nonadiabatic Quantum Molecular Dynamics. *Chem. Rev.* **2018**, *118*, 3305–3336.
- (18) Ben-Nun, M.; Martínez, T. J. Ab Initio Quantum Molecular Dynamics. In *Advances in Chemical Physics*; John Wiley & Sons, Inc., 2002; pp 439–512.
- (19) Yu, J. K.; Bannwarth, C.; Liang, R.; Hohenstein, E. G.; Martínez, T. J. Nonadiabatic Dynamics Simulation of the Wavelength-

- Dependent Photochemistry of Azobenzene Excited to the $n\pi^*$ and $\pi\pi^*$ Excited States. *J. Am. Chem. Soc.* **2020**, *142*, 20680–20690.
- (20) Liang, R. First-Principles Nonadiabatic Dynamics Simulation of Azobenzene Photodynamics in Solutions. *J. Chem. Theory Comput.* **2021**, *17*, 3019–3030.
- (21) Liang, R.; Das, D.; Bakhtiari, A. Protein confinement fine-tunes aggregation-induced emission in human serum albumin. *Phys. Chem. Chem. Phys.* **2021**, *23*, 26263–26272.
- (22) Mondal, P.; Granucci, G.; Rastädter, D.; Persico, M.; Burghardt, I. Azobenzene as a photoregulator covalently attached to RNA: a quantum mechanics/molecular mechanics-surface hopping dynamics study. *Chem. Sci.* **2018**, *9*, 4671–4681.
- (23) Mondal, P.; Biswas, M.; Goldau, T.; Heckel, A.; Burghardt, I. In Search of an Efficient Photoswitch for Functional RNA: Design Principles from a Microscopic Analysis of Azobenzene-linker-RNA Dynamics with Different Linkers. *J. Phys. Chem. B* **2015**, *119*, 11275–11286.
- (24) Xia, S.-H.; Cui, G.; Fang, W.-H.; Thiel, W. How Photoisomerization Drives Peptide Folding and Unfolding: Insights from QM/MM and MM Dynamics Simulations. *Angew. Chem. Int.* **2016**, *55*, 2067–2072.
- (25) Tully, J. C. Molecular dynamics with electronic transitions. *J. Chem. Phys.* **1990**, *93*, 1061–1071.
- (26) Bittner, E. R.; Rossky, P. J. Quantum decoherence in mixed quantum-classical systems: Nonadiabatic processes. *J. Chem. Phys.* **1995**, *103*, 8130–8143.
- (27) Ibele, L. M.; Lassmann, Y.; Martínez, T. J.; Curchod, B. F. E. Comparing (stochastic-selection) ab initio multiple spawning with trajectory surface hopping for the photodynamics of cyclopropanone, fulvene, and dithiane. *J. Chem. Phys.* **2021**, *154*, No. 104110.
- (28) Wang, L.; Qiu, J.; Bai, X.; Xu, J. Surface hopping methods for nonadiabatic dynamics in extended systems. *Wiley Interdiscip. Rev. Comput. Mol. Sci.* **2020**, *10*, No. e1435.
- (29) Cody, V.; Luft, J. R.; Pangborn, W. Understanding the role of Leu22 variants in methotrexate resistance: comparison of wild-type and Leu22Arg variant mouse and human dihydrofolate reductase ternary crystal complexes with methotrexate and NADPH. *Acta Crystallogr., Sect. D* **2005**, *61*, 147–155.
- (30) Maier, J. A.; Martínez, C.; Kasavajhala, K.; Wickstrom, L.; Hauser, K. E.; Simmerling, C. ff14SB: Improving the Accuracy of Protein Side Chain and Backbone Parameters from ff99SB. *J. Chem. Theory Comput.* **2015**, *11*, 3696–3713.
- (31) Dickson, C. J.; Madej, B. D.; Skjerve, Å. A.; Betz, R. M.; Teigen, K.; Gould, I. R.; Walker, R. C. Lipid14: The Amber Lipid Force Field. *J. Chem. Theory Comput.* **2014**, *10*, 865–879.
- (32) Lee, C.; Yang, W.; Parr, R. G. Development of the Colle-Salvetti correlation-energy formula into a functional of the electron density. *Phys. Rev. B* **1988**, *37*, 785–789.
- (33) Bayly, C. I.; Cieplak, P.; Cornell, W.; Kollman, P. A. A well-behaved electrostatic potential based method using charge restraints for deriving atomic charges: the RESP model. *J. Phys. Chem. A* **1993**, *97*, 10269–10280.
- (34) Trott, O.; Olson, A. J. AutoDock Vina: Improving the speed and accuracy of docking with a new scoring function, efficient optimization, and multithreading. *J. Comput. Chem.* **2010**, *31*, 455–461.
- (35) Wang, J.; Wolf, R. M.; Caldwell, J. W.; Kollman, P. A.; Case, D. A. Development and testing of a general amber force field. *J. Comput. Chem.* **2004**, *25*, 1157–1174.
- (36) Wang, J.; Wang, W.; Kollman, P. A.; Case, D. A. Automatic atom type and bond type perception in molecular mechanical calculations. *J. Mol. Graph. Model.* **2006**, *25*, 247–260.
- (37) Wu, Y. J.; Tepper, H. L.; Voth, G. A. Flexible simple point-charge water model with improved liquid-state properties. *J. Chem. Phys.* **2006**, *124*, No. 024503.
- (38) Eastman, P.; Friedrichs, M. S.; Chodera, J. D.; Radmer, R. J.; Bruns, C. M.; Ku, J. P.; Beauchamp, K. A.; Lane, T. J.; Wang, L.-P.; Shukla, D.; et al. OpenMM 4: A Reusable, Extensible, Hardware Independent Library for High Performance Molecular Simulation. *J. Chem. Theory Comput.* **2013**, *9*, 461–469.
- (39) Ufimtsev, I. S.; Martinez, T. J. Quantum Chemistry on Graphical Processing Units. 3. Analytical Energy Gradients, Geometry Optimization, and First Principles Molecular Dynamics. *J. Chem. Theory Comput.* **2009**, *5*, 2619–2628.
- (40) Titov, A. V.; Ufimtsev, I. S.; Luehr, N.; Martinez, T. J. Generating Efficient Quantum Chemistry Codes for Novel Architectures. *J. Chem. Theory Comput.* **2013**, *9*, 213–221.
- (41) Seritan, S.; Bannwarth, C.; Fales, B. S.; Hohenstein, E. G.; Kokkila-Schumacher, S. I. L.; Luehr, N.; Snyder, J. W.; Song, C.; Titov, A. V.; Ufimtsev, I. S.; et al. TeraChem: Accelerating electronic structure and ab initio molecular dynamics with graphical processing units. *J. Chem. Phys.* **2020**, *152*, No. 224110.
- (42) Seritan, S.; Bannwarth, C.; Fales, B. S.; Hohenstein, E. G.; Isborn, C. M.; Kokkila-Schumacher, S. I. L.; Li, X.; Liu, F.; Luehr, N.; Snyder, J. W., Jr; et al. TeraChem: A graphical processing unit-accelerated electronic structure package for large-scale ab initio molecular dynamics. *Wiley Interdiscip. Rev. Comput. Mol. Sci.* **2021**, *11*, No. e1494.
- (43) Haghdani, S.; Davari, N.; Sandnes, R.; Åstrand, P.-O. Complex Frequency-Dependent Polarizability through the $\pi \rightarrow \pi^*$ Excitation Energy of Azobenzene Molecules by a Combined Charge-Transfer and Point-Dipole Interaction Model. *J. Phys. Chem. A* **2014**, *118*, 11282–11292.
- (44) Gozem, S.; Luk, H. L.; Schapiro, I.; Olivucci, M. Theory and Simulation of the Ultrafast Double-Bond Isomerization of Biological Chromophores. *Chem. Rev.* **2017**, *117*, No. 13502.
- (45) Barbatti, M.; Aquino, A. J. A.; Lischka, H. The UV absorption of nucleobases: semi-classical ab initio spectra simulations. *Phys. Chem. Chem. Phys.* **2010**, *12*, 4959–4967.
- (46) Curchod, B. F. E.; Glover, W. J.; Martínez, T. J. SSAIMS—Stochastic-Selection Ab Initio Multiple Spawning for Efficient Nonadiabatic Molecular Dynamics. *J. Phys. Chem. A* **2020**, *124*, 6133–6143.
- (47) Yarkony, D. R. Nuclear dynamics near conical intersections in the adiabatic representation: I. The effects of local topography on interstate transitions. *J. Chem. Phys.* **2001**, *114*, 2601–2613.
- (48) Kumar, S.; Bouzida, D.; Swendsen, R. H.; Kollman, P. A.; Rosenberg, J. M. The Weighted Histogram Analysis Method for Free-Energy Calculations on Biomolecules. 1. The Method. *J. Comput. Chem.* **1992**, *13*, 1011–1021.
- (49) Kumar, S.; Rosenberg, J. M.; Bouzida, D.; Swendsen, R. H.; Kollman, P. A. Multidimensional Free-Energy Calculations Using the Weighted Histogram Analysis Method. *J. Comput. Chem.* **1995**, *16*, 1339–1350.
- (50) Bortolus, P.; Monti, S. Cis-trans photoisomerization of azobenzene. Solvent and triplet donors effects. *J. Phys. Chem. B* **1979**, *83*, 648–652.
- (51) Ladányi, V.; Dvořák, P.; Al Anshori, J.; Vetráková, L.; Wirz, J.; Heger, D. Azobenzene photoisomerization quantum yields in methanol redetermined. *Photochem. Photobiol. Sci.* **2017**, *16*, 1757–1761.
- (52) Gauglitz, G.; Hubig, S. Chemical actinometry in the UV by azobenzene in concentrated solution: A convenient method. *J. Photochem.* **1985**, *30*, 121–125.
- (53) Ronayette, J.; Arnaud, R.; Lebourgeois, P.; Lemaire, J. Isomérisation photochimique de l'azobenzène en solution. I. *Can. J. Chem.* **1974**, *52*, 1848–1857.
- (54) Aleotti, F.; Nenov, A.; Salvigni, L.; Bonfanti, M.; El-Tahawy, M. M.; Giunchi, A.; Gentile, M.; Spallacci, C.; Ventimiglia, A.; Cirillo, G.; et al. Spectral Tuning and Photoisomerization Efficiency in Push–Pull Azobenzenes: Designing Principles. *J. Phys. Chem. A* **2020**, *124*, 9513–9523.
- (55) Aleotti, F.; Soprani, L.; Nenov, A.; Berardi, R.; Arcioni, A.; Zannoni, C.; Garavelli, M. Multidimensional Potential Energy Surfaces Resolved at the RASPT2 Level for Accurate Photoinduced Isomerization Dynamics of Azobenzene. *J. Chem. Theory Comput.* **2019**, *15*, 6813–6823.

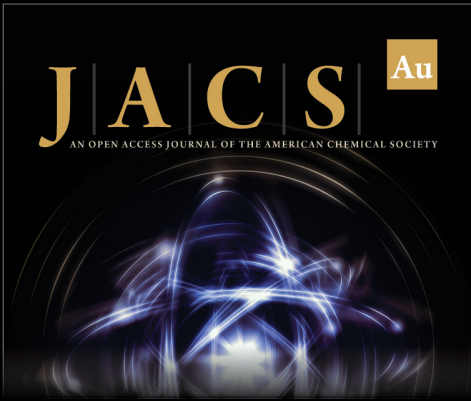
(56) Granucci, G.; Persico, M. Excited state dynamics with the direct trajectory surface hopping method: azobenzene and its derivatives as a case study. *Theor. Chem. Acc.* **2007**, *117*, 1131–1143.

(57) Ciminelli, C.; Granucci, G.; Persico, M. The Photoisomerization Mechanism of Azobenzene: A Semiclassical Simulation of Nonadiabatic Dynamics. *Chem. - Eur. J.* **2004**, *10*, 2327–2341.

(58) Liu, L.; Liu, J.; Martinez, T. J. Dynamical Correlation Effects on Photoisomerization: Ab Initio Multiple Spawning Dynamics with MS-CASPT2 for a Model trans-Protonated Schiff Base. *J. Phys. Chem. B* **2016**, *120*, 1940–1949.

(59) Liang, R.; Yu, J. K.; Meisner, J.; Liu, F.; Martinez, T. J. Electrostatic Control of Photoisomerization in Channelrhodopsin 2. *J. Am. Chem. Soc.* **2021**, *143*, 5425–5437.

(60) Kingsland, A.; Samai, S.; Yan, Y.; Ginger, D. S.; Maibaum, L. Local Density Fluctuations Predict Photoisomerization Quantum Yield of Azobenzene-Modified DNA. *J. Phys. Chem. Lett.* **2016**, *7*, 3027–3031.



JACS Au
AN OPEN ACCESS JOURNAL OF THE AMERICAN CHEMICAL SOCIETY

 Editor-in-Chief
Prof. Christopher W. Jones
Georgia Institute of Technology, USA

Open for Submissions 

pubs.acs.org/jacsau  ACS Publications
Most Trusted. Most Cited. Most Read.